Solar Phys (2008) 249: 233–261
DOI 10.1007/s11207-008-9169-9

Polarization Calibration of the Solar Optical Telescope onboard *Hinode*

K. Ichimoto · B. Lites · D. Elmore · Y. Suematsu · S. Tsuneta · Y. Katsukawa · T. Shimizu · R. Shine · T. Tarbell · A. Title · J. Kiyohara · K. Shinoda · G. Card · A. Lecinski · K. Streander · M. Nakagiri · M. Miyashita · M. Noguchi · C. Hoffmann · T. Cruz

Received: 12 June 2007 / Accepted: 7 March 2008 / Published online: 5 April 2008

Abstract The Solar Optical Telescope (SOT) onboard *Hinode* aims to obtain vector magnetic fields on the Sun through precise spectropolarimetry of solar spectral lines with a spatial resolution of 0.2 – 0.3 arcsec. A photometric accuracy of 10^{-3} is achieved and, after the polarization calibration, any artificial polarization from crosstalk among Stokes parameters is required to be suppressed below the level of the statistical noise over the SOT's field of view. This goal was achieved by the highly optimized design of the SOT as a polarimeter, extensive analyses and testing of optical elements, and an end-to-end calibration test of the entire system. In this paper we review both the approach adopted to realize the high-precision polarimeter of the SOT and its final polarization characteristics.

Keywords Polarimeter · Stokes vector · Space telescope · Magnetic field · Optical telescope · Sun

K. Ichimoto (✉) · Y. Suematsu · S. Tsuneta · Y. Katsukawa · K. Shinoda · M. Nakagiri · M. Miyashita · M. Noguchi
National Astronomical Observatory of Japan, 2-21-1, Osawa, Mitaka, Toyko 181-8588, Japan
e-mail: ichimoto@solar.mtk.nao.ac.jp

B. Lites · D. Elmore · G. Card · A. Lecinski · K. Streander
High Altitude Observatory, National Center for Atmospheric Research, P.O. Box 3000 Boulder, CO 80307-3000, USA

R. Shine · T. Tarbell · A. Title · C. Hoffmann · T. Cruz
Lockheed Martin Advanced Technology Center, 3251 Hanover Street, Palo Alto, CA 94304, USA

T. Shimizu
Japan Aerospace Exploration Agency, Institute of Space and Astronautical Science, 3-1-1, Yoshinodai, Sagamihara, Kanagawa 229-8510, Japan

J. Kiyohara
Kwasan Observatory, Kyoto University, Kita-Kazan Ohmine-cho, Yamashina-ku, Kyoto 607-8471, Japan

1. Introduction

The science goals of the Solar Optical Telescope (SOT; Tsuneta *et al.*, 2008) onboard *Hinode* (formerly *Solar-B*; Shimizu, 2004; Ichimoto *et al.*, 2005; Kosugi *et al.*, 2007) require high-precision polarimetry of solar spectral lines with a spatial resolution of 0.2 – 0.3 arcsec. *Hinode*/SOT thus provides the first quantitative and continuous measurements of full vector magnetic fields of the Sun that either resolve or isolate the solar fine-scale magnetic structures. The Focal Plane Package (FPP) of the SOT contains two sets of vector magnetographs (Tarbell *et al.*, 2008). The Spectropolarimeter (SP) performs the highest precision polarimetry with a photometric accuracy of $\approx 10^{-3}$ to provide full Stokes profiles of Fe I 630.25/630.15 nm lines with a spatial sampling of 0.16 arcsec. The Narrowband Filter Imager (NFI) of Filtergraph (FG), in contrast, produces two-dimensional images of Stokes parameters using a Lyot-type tunable filter (width ≈ 0.1 Å) in several photospheric and chromospheric lines with spatial sampling of 0.08″/pixel and higher time cadence, but with lower wavelength resolution. The available spectral bands of the NFI contain Fe I 630.2/630.1/525.0/524.7 nm for photospheric magnetograms, Na I 589.6/Mg I 517.2 nm for chromospheric magnetogram/Dopplergrams, Fe I 557.6 nm for photospheric Dopplergrams, and H I 656.3 nm for chromospheric images/Dopplergrams. Both the SP and the NFI have a field of view (FOV) of 328×164 arcsec^2.

One of the most significant sources of error in high-spatial-resolution ground-based solar polarimetry is noise caused by atmospheric seeing. Since seeing produces rapid image motion, blurring, and distortion, if the polarization modulation is slower than 1000 Hz, seeing causes false "polarization" signals. Furthermore, attaining high spectropolarimetric precision (10^{-3} relative to the continuum intensity, I_c) at the telescope resolution demands integration times of at least several seconds. Even with adaptive optical correction, atmospheric seeing can significantly degrade image quality. As a result, an accuracy of 10^{-3} in Stokes vector measurements has rarely been achieved at a spatial resolution of less than 1 arcsec, and then never for an extended period of time. *Hinode*/SOT overcomes this difficulty by flying the telescope in space and stabilizing the residual pointing error with an image stabilization system (Shimizu *et al.*, 2004, 2008). The next major source of the error in polarization measurement is the instrumental polarization. Most large ground-based solar telescopes employ feed optics with oblique, time-varying reflective angles, which introduce considerable time variation in the instrumental polarization. In contrast, the SOT consists of symmetric optical system with constant, small-angle reflections. Since the entire observatory (satellite) points to the Sun, the instrumental polarization of *Hinode*/SOT is small and nearly constant. However, because on-orbit polarization calibration of the instruments and telescope is impractical, and because the SOT is exposed to significant thermal variation, a major design effort and comprehensive polarization tests of the system were required prior to launch.

In this paper, we review the methodology used for calibrating the SOT polarization and describe the final characteristics of the SOT polarimeter. The overview of the SOT as a polarimeter is described in Section 2, the goal of polarization calibration accuracy is defined quantitatively in Section 3, some component-level calibration tests are described in Section 4, and system calibration using the final SOT configuration is described in Section 5. Characterization and modeling of SOT polarization is discussed in Section 6 with additional information on data sampling schemes in Section 7. Section 8 summarizes the conclusions.

2. Overview of the SOT Polarimeter

Figure 1 presents a schematic diagram of the SOT optical system, emphasizing those components essential to polarimetry. The Optical Telescope Assembly (OTA; Ichimoto *et al.*, 2004; Suematsu *et al.*, 2008) is a 50-cm-aperture Gregorian telescope containing the primary mirror, secondary mirror, collimator lens unit (CLU), polarization modulator unit (PMU), tip-tilt folding mirror (CTM-TM), and astigmatism corrector lens (ACL) as elements that may act on the polarization states of the incident light. The primary and secondary mirrors have ellipsoidal figures and protected silver coatings. The CLU is an achromatic lens unit that consists of six elements of different types of optical glasses. The CLU provides a collimated beam to the FPP and creates a 30-mm ϕ pupil image between the CTM-TM and the ACL. The ACL is a nearly plane parallel silica plate with a thickness of 10 mm. This plate was installed after assembly and testing of the Gregorian telescope to eliminate the as-built small astigmatism of the telescope (see Suematsu *et al.*, 2008). To prevent a ghost from a reflection of the collimated beam, the plate was tilted by 1.5 degrees with respect to the optical axis. The PMU is a bicrystalline athermal waveplate that rotates at a constant rate of 1/1.6 Hz. Retardation is optimized for measurements of both circular and linear polarization at 630.2 and 517.2 nm (Guimond and Elmore, 2004). The beam is split between the SP and the FG paths by a nonpolarizing beam splitter. The polarizer in front of the tunable filter and a polarizing beam splitter in front of the SP CCD provide the polarization analysis for FG/NFI and SP, respectively.

Both SP-CCD and FG-CCD take multiple images synchronously with the PMU. The SP takes 16 exposures for each PMU revolution in both orthogonally polarized beams. The FG has a variety of sampling schemes. In the "shuttered mode" of the NFI, the mechanical shutter is used to control the exposure of a large area of the CCD. The mechanical shutter

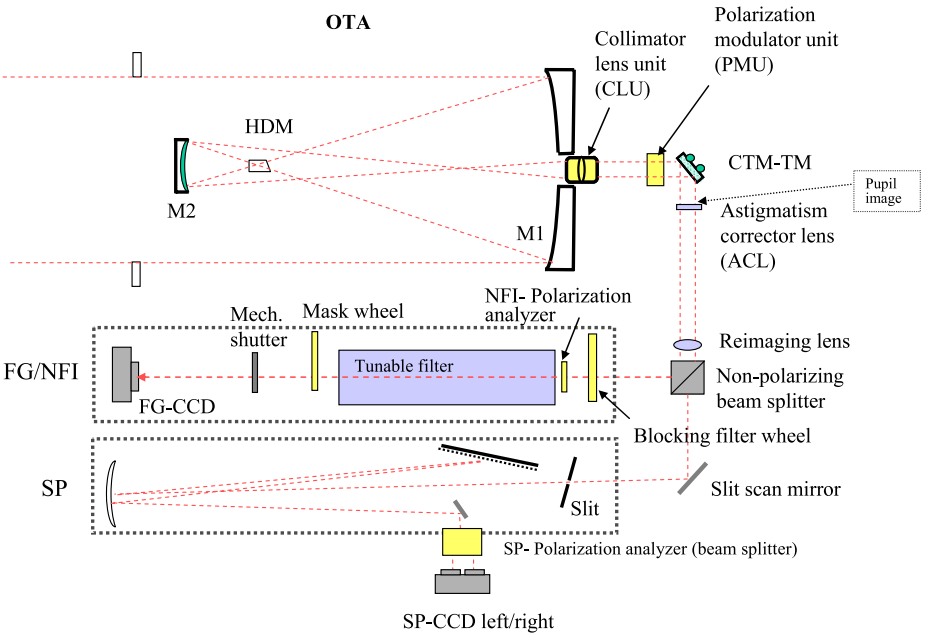

Figure 1 Schematic of the SOT polarimeter.

is placed at a pupil image to avoid PMU phase variation across the field of view during exposures. In "shutterless mode," continuous readout is performed in the central area of the CCD. The mask wheel located at an intermediate focus has a selectable aperture that masks off different amounts of the outer portions of the CCD. Appropriate demodulation (successive addition and subtraction of images) is applied onboard for each sampling sequence to reduce data telemetry volume data and to improve signal to noise (S/N). The SOT data products are then I, Q, U, and V images, which require further correction by a calibration matrix to obtain the Stokes vector of the light incident to the telescope. Typical sampling schemes of the NFI are as follows:

In shuttered mode:
8 exposures at 22.5° waveplate rotation intervals for $IQUV$.
4 exposures for $IQUV$.
2 exposures for IV.
Other exposure schemes are also possible with variable exposure times.
In shutterless mode:
16 frames/rev. for $IQUV$ (same as SP).
4 frames/half rev. for IV.
2 frames/half rev. for IV.
Other exposure schemes are also possible with flexible numbers of accumulations.

The key features that optimize the SOT as a polarimeter are summarized as follows:

1. Axisymmetric configuration up to the polarization modulator: As shown in the next section, the optical system up to the polarization modulator is most critical to the accurate measurement of polarization. The axisymmetric configuration of this system is a great advantage for minimizing the crosstalk among the Stokes $IQUV$.
2. Simple rotating waveplate for the polarization modulator: Since a rotating waveplate causes Stokes Q, U, and V to be modulated at different frequencies and phases, the crosstalk among them is not sensitive to the absolute retardation of the waveplate.
3. Rotating waveplate located near the pupil image: Any possible defect or nonuniformity of the waveplate will not produce spurious intensity modulation at the detector.
4. Simultaneous measurements of both orthogonally polarized beams at the SP-CCD: Any residual guiding error of the spacecraft will produce an intensity modulation. This term (I to QUV crosstalk) may be greatly reduced by combining observables taken simultaneously in the two orthogonal polarizations.

3. Requirement on Accuracy of the Polarization Calibration

The "polarimeter response matrix" $\mathbf{X}$ (Elmore, 1990) is defined as $\mathbf{S}' = \mathbf{X}\mathbf{S}$, where $\mathbf{S}$ is the incident Stokes vector to the telescope and $\mathbf{S}'$ is the data product of the SOT (demodulated intensity; see Figure 2). Our goal of the polarization calibration of the SOT is to determine the $\mathbf{X}$ matrix of both the SP and the FG/NFI with a required accuracy as described in the following. For the crosstalk among different elements of the Stokes vector, we require that a fictitious signal produced by the incorrect evaluation of $\mathbf{X}$ should be smaller than the statistical noise (photon noise). Denoting the polarimeter response matrix used in data reduction as $\mathbf{X}_\mathrm{r}$, we can write the error in the reduced Stokes vector as

$$\Delta\mathbf{S} = \mathbf{S}'' - \mathbf{S} = \mathbf{X}_\mathrm{r}^{-1}\mathbf{S}' - \mathbf{S} = \left(\mathbf{X}_\mathrm{r}^{-1}\mathbf{X} - \mathbf{E}\right)\mathbf{S},$$

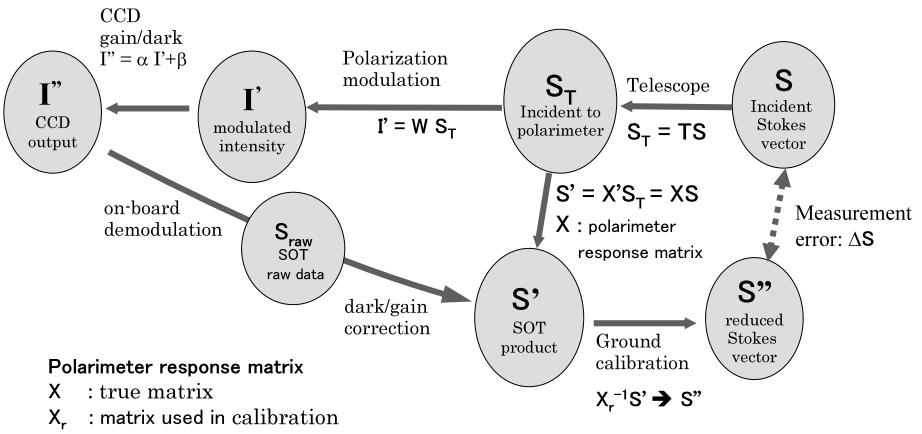

Figure 2 Definition of polarization response matrix and error in polarization measurements.

where $\mathbf{S}''$ is the reduced Stokes vector, $\mathbf{X}$ is the real, but unknown, polarimeter response matrix, and $\mathbf{E}$ is the identity matrix. The error in the reduced Stokes vector from the statistical noise, ε, is given by

$$\delta\mathbf{S} = \mathbf{X}_{\mathrm{r}}^{-1}\delta\mathbf{S}' = \mathbf{X}_{\mathrm{r}}^{-1}\boldsymbol{\varepsilon},$$

where $\boldsymbol{\varepsilon}$ is a four-element column vector with all elements having a value of ε.

The requirement of $\Delta\mathbf{S} < \delta\mathbf{S}$ reduces to

$$\Delta\mathbf{X}\mathbf{S} < \boldsymbol{\varepsilon},$$

where $\Delta\mathbf{X} \equiv (\mathbf{X} - \mathbf{X}_{\mathrm{r}})$ is the required accuracy for $\mathbf{X}$. This inequality is interpreted as follows: Let p_{l} and p_{c} denote the maximum linear and circular polarizations, respectively, in realistic spectral lines from the Sun. When one applies $\Delta\mathbf{X}$ to the Stokes vectors representing the anticipated maximum polarization (*i.e.*, $\mathbf{S} = (1, p_{\mathrm{l}}, 0, 0)^{\mathrm{T}}$, $(1, 0, p_{\mathrm{l}}, 0)^{\mathrm{T}}$, or $(1, 0, 0, p_{\mathrm{c}})^{\mathrm{T}}$ incident to the telescope), the resulting error of each Stokes parameter should be smaller than ε. In particular, off-diagonal elements of $\Delta\mathbf{X}$ produce a false signal of a Stokes component even when the component is intrinsically zero via the crosstalk from other Stokes components. Such errors must be suppressed below the detection limit of the system (*i.e.*, ε). However, the "scale error," which is introduced by the error of diagonal elements or the first row of $\mathbf{X}$, does not produce a false signal of a Stokes component if that component is intrinsically zero, but changes its value with a certain factor. Since the scale error exists also in derivations of the magnetic fields from the Stokes profiles of spectral lines because of uncertainties in solar atmospheric models, we relax the requirement on the scale errors and set the limit by an "uncertainty factor" a rather than ε. After normalizing $\mathbf{S}$ by the intensity ($I = 1$ and $x_{11} = 1$, we can write the inequality for $\Delta\mathbf{X}$ as

$$|\Delta\mathbf{X}| < \begin{pmatrix} - & a/p_{\mathrm{l}} & a/p_{\mathrm{l}} & a/p_{\mathrm{v}} \\ \varepsilon & a & \varepsilon/p_{\mathrm{l}} & \varepsilon/p_{\mathrm{v}} \\ \varepsilon & \varepsilon/p_{\mathrm{l}} & a & \varepsilon/p_{\mathrm{v}} \\ \varepsilon & \varepsilon/p_{\mathrm{l}} & \varepsilon/p_{\mathrm{l}} & a \end{pmatrix}.$$

Table 1 Classification of polarimeter components.

	Definition	SOT components	
M_T	Elements before polarization modulator	Gregorian telescope, CLU	
M_P	Polarization modulator	Rotating waveplate (PMU)	
M_B	Elements between polarization modulator and analyzer	Tip-tilt mirror, reimaging lens, beam splitter	
		(SP)	(NFI)
		Scanning mirror	Folding mirrors
		Blocking filter	
		Slit	
		Field lens	
		spectrograph	
M_A	Polarization analyzer	Polarizing beam splitter	Polarizer
M_F	Elements following the polarization analyzer	CCD	Filters
			Relay lenses
			Folding mirror
			CCD

In case of *Hinode*/SOT, we adopt the following values:

$$\varepsilon = 0.001,$$
$$a = 0.05,$$
$$P_l = 0.15 \quad (\text{max of } Q, U),$$
$$P_c = 0.2 \quad (\text{max of } V),$$

and hence the tolerance of $\mathbf{X}$ becomes

$$|\Delta\mathbf{X}| < \begin{pmatrix} - & 0.333 & 0.333 & 0.250 \\ 0.001 & 0.050 & 0.007 & 0.005 \\ 0.001 & 0.007 & 0.050 & 0.005 \\ 0.001 & 0.007 & 0.007 & 0.050 \end{pmatrix}.$$

This relation gives the basis of our goal of the SOT polarization calibration.

The optical components in a polarimeter can be classified into five groups based on their location in the optical system with respect to the polarization modulator and the analyzer. Table 1 shows the category of the polarization elements in the SOT. The tolerances of polarization properties of components in each group may be evaluated using the tolerance matrix $\Delta\mathbf{X}$ specified here; that is, one may calculate the amount of error in diattenuation, retardation, or depolarization of each of the elements that causes the error of one of the elements of $\mathbf{X}$ to exceed the tolerance $\Delta\mathbf{X}$. Table 2 shows these calculated tolerances of the polarization properties for each group.

It is obvious from Table 2 that the first elements in the optical train have the tightest tolerance limits and components in the OTA need to be carefully characterized for their

Table 2 Tolerance of polarization properties for each component.

Location	Diattenuation	Retardation (deg)	Orientation (deg)	Depolarization
M_T	0.0010 ($I \rightarrow Q, U$)	0.286 ($V \rightarrow U$)	Does not matter	0.050 (dQ, U, V)
M_P	0.0053 ($U \rightarrow V$)	3.687 (dV)	0.095 (Q–U)	0.050 (dQ, U, V)
M_B	0.0073* (Q–U)	0.419* ($Q \rightarrow V$)	0.100 (U–Q)	0.050 (dQ, U, V)
M_A	Does not matter	Does not matter	0.233 (Q–U)	Does not matter
M_F	Does not matter	Does not matter	2.100 (Q–U)	Does not matter

Note. The kind of crosstalk that limits the tolerance of each error is shown in parentheses.

*The axis of error is assumed to be 45° to the axis of the polarization analyzer. Off-axis rays from the edge of the FOV entering on the CTM-TM or the BS correspond to an axis rotation of $\approx 0.7°$.

polarization properties. In the measurements of **X** matrices of the SOT, the uniformity of the **X** matrices over the field of view and their temperature stability are also important aspects to be characterized. In the next section, we focus on polarization calibration of the critical components of the OTA (*i.e.*, optical coatings and the CLU).

4. Component Calibration

In the development of the SOT, the highest priorities for design of optical components and selection of materials were their durability in the space environment and ability to achieve high wavefront quality. Where choices were possible (*e.g.*, optical coatings, waveplate design, *etc.*), polarization properties were also a major factor for the selection. The expected polarization characteristics of each component in a realistic space thermal environment was studied based on theoretical properties in the design phase. After the fabrication of each component, polarization properties were measured and characterized using the Component Polarization Analyzer (CPA) developed by HAO. The CPA consists of a "polarization generator" and a "polarization analyzer" with a sample to be measured in between them. The former creates known polarized lights (a set of Stokes vectors) and the later measures the Stokes vectors of the light after passage through the sample. The spatial distributions of 16 elements of the Mueller matrix of the sample can be obtained as two-dimensional maps with an accuracy that meets our requirement. In this section, examples of component polarization calibration are described for representative cases that are the most critical for accurate polarimetry with the SOT (*i.e.*, optical coatings in the OTA and the CLU).

4.1. Optical Coatings in the OTA

Coatings on mirrors or lenses can directly affect the polarization state of the beam, and those in the OTA are especially critical for the final performance of the polarimeter. The primary and secondary mirrors are 1170- and 263-mm focal length ellipsoids with a protected silver coating provided by SAGEM/REOSC. The CLU is a six-element achromatic lens schematically drawn in Figure 3. All elements have an antireflection coating on their surfaces provided by Canon, except for the first surface, which has a bandpass coating to reject most IR and ultraviolet wavelengths. The coating was fabricated by the Ion Beam Spattering system of NAOJ. There are in total 14 optical surfaces before the light reaches the PMU. Figure 4 shows the maximum incidence angles of the rays from the center and

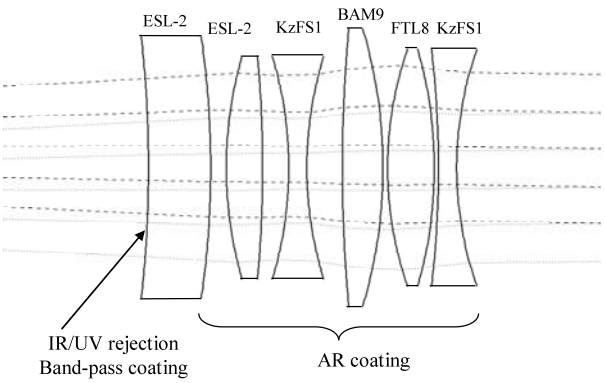

Figure 3 Configuration of CLU with coatings on each surface.

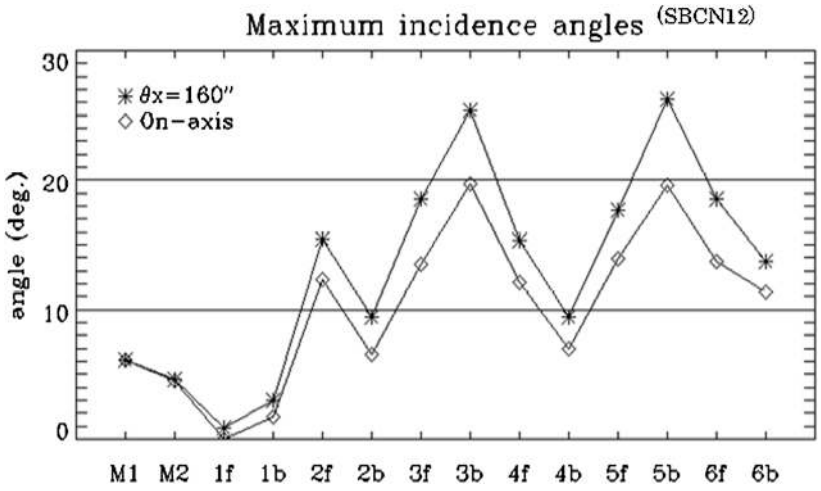

Figure 4 Maximum incidence angle of rays at each surface of M1, M2, and CLU.

edge of the field of view at each surface. Since the CLU is optically rather fast, these angles are up to 26° for particular rays at the edge of the FOV.

Figure 5 shows the theoretical polarization properties of the protected silver coating on M1 and M2 (left) and the antireflection coating of one of the CLU elements (right) as a function of incident angle. Shown from top to bottom are the transmission of P and S polarizations, diattenuation, and retardation. These properties were evaluated by using the actual measurements of coating witness samples by the CPA. Examples of the results are shown with error bars in the right panel of Figure 5. It should be remarked that the most significant outcome from the measurements is the confirmation that there is neither unexpected retardation nor diattenuation at normal incidence. Actually, we found that some coatings, which were deposited under anisotropic conditions, can have such behavior, and one coating that had an "intrinsic" polarization was rejected in the development of the SOT.

To evaluate the net polarization of the telescope from the optical coatings, a polarizing ray tracing was performed in which the propagation of the Stokes vectors (or Jones vectors) of individual rays were calculated based on the polarization properties of the coatings. The rays were combined after passing through the optics. Because of the axisymmetric configuration

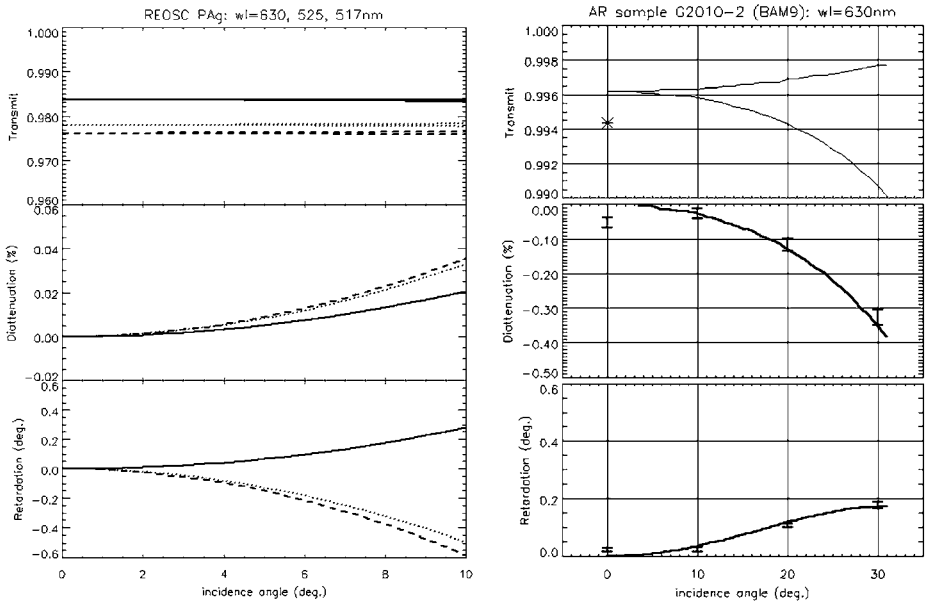

Figure 5 Theoretical polarization properties of the protected silver coating on M1 and M2 (left) and the antireflection coating of one of the CLU elements (right) as a function of incident angle: transmission of P and S polarizations (top), diattenuation (middle), and retardation (bottom). Shown are curves for a protected silver coating at 517 nm (dashed), 525 nm (dotted), and 630 nm (solid). In the right panel, measurement results are also shown with error bars.

of the telescope, the net polarization is theoretically zero at the center of the field of view, and the Gregorian telescope ($M1 + M2$) has diattenuation and retardation of the order of 10^{-8} and 10^{-4} degrees at the edge of FOV, respectively (both of which are much smaller than our tolerance). Figure 6 shows an example of calculations for the CLU at the edge of the FOV. Short lines correspond to the rays incident at different points on the pupil. The length and direction of each line show the amount and direction of the diattenuation resulting from the 12 surfaces of the CLU. After combining these rays, one obtains the net diattenuation and retardation of the CLU coatings: about 3×10^{-4} and 0.08°, both of which, again, are smaller than our requirements given in Table 2.

4.2. CLU Optothermal Properties

The six elements of the CLU are tightly mounted in a titanium housing to maintain their precise positions and survive the launch load. (For details of the CLU design, see Suematsu *et al.* (2008).) In contrast to reflective surfaces, at the CLU, light passes through the optical media, which may have internal stress. Thus the CLU polarization may be quite sensitive to the properties of the optical glasses and also temperature since the mechanical stress on the glasses induced from the titanium housing may cause additional retardation. This led us to perform extensive analyses and testing to characterize the optothermal polarization properties of the CLU.

Prior to fabrication of the CLU, we measured the retardation of the glass blanks for all lens elements caused by the residual internal stress and also the stress-optical coefficients of the optical glasses using a HeNe laser at 632.8 nm. Table 3 summarizes the results of

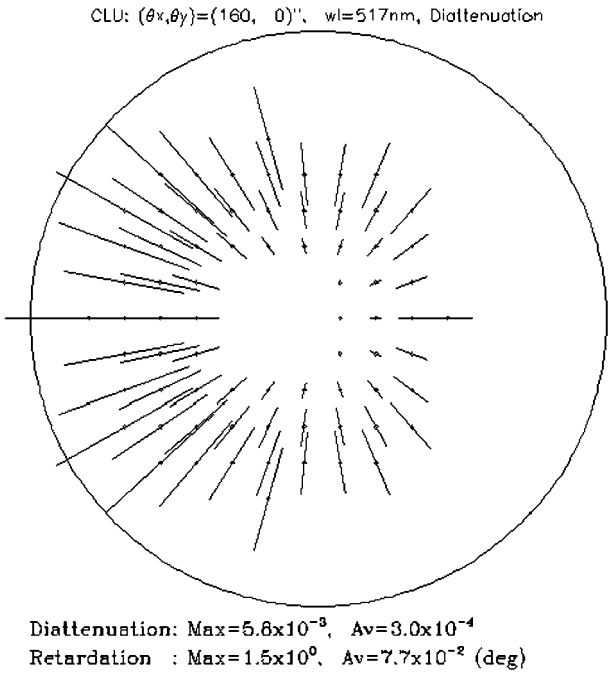

Figure 6 Result of polarizing ray tracing for the CLU for the rays at the edge of the SOT field of view (see text for details).

Table 3 Optomechanical properties of the CLU glasses (measurements by NAOJ).

	Retardation due to the internal stress (degree cm^{-1} @630 nm)	Stress-optical coeff. ($\times 10^{-6}$ mm^2 N^{-1})	Supplier
BAM9	0.033 – 0.035	1.89	Ohara
KzFS1	0.441 – 0.632	3.52	Schott
FTL8	0.087 – 0.123	3.17	Ohara
ESL2 (silica)	0.110 – 0.148	3.37	Tosoh

the measurements. We selected the glass blank that has a minimum retardation for the flight CLU, and, for the KzFS1, for which all blanks have non-negligible retardation, we aligned the axes of retardation of two KzFS1 elements in the CLU orthogonally to cancel the retardations. By performing extensive thermomechanical analyses, we calculated the internal stress distributions of each CLU element under realistic thermal conditions with the absorption of incident solar light, and, using the measured stress-optical coefficients, we evaluated the retardation of the CLU. The promising result indicated a small polarization effect of the CLU, but the simulation was based on an ideal axisymmetric mechanical model of the CLU.

Tests of polarization properties with the real flight CLU were performed by using the CPA. The CLU was mounted in a thermal shroud and put in a beam that simulates the flight optical configuration, and the Mueller matrix was obtained as a function of position in the FOV at $\lambda = 630.2$ nm under various temperature conditions before and after mechanical load and thermal cycling tests. Figure 7 shows examples of two-dimensional images of the Mueller matrix elements derived from the CPA measurement, where the temper-

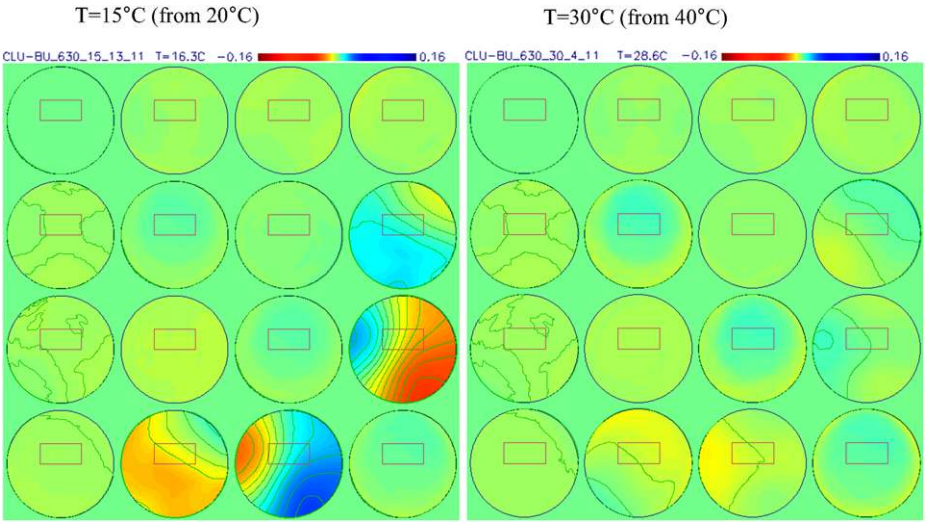

Figure 7 Mueller matrix image of the CLU at $T = 15°\mathrm{C}$ (left) and $T = 30°\mathrm{C}$ (right) as inferred from CPA measurements. Rectangles in each matrix element show the SOT field of view. The contour intervals indicate the tolerance of each Mueller matrix element.

ature of the CLU was 15°C (left) and 30°C (right). Each image spans different incident ray angles and the rectangle in each matrix element shows the SOT field of view. Contour intervals indicate the tolerance of each Mueller matrix element as defined in Section 3. We observe a clear indication of large, inhomogeneous polarization effects when the CLU temperature is low, especially in two elements in the last row ($[2, 4]$ and $[3, 4]$) and two elements in the last column ($[4, 2]$ and $[4, 3]$), which correspond to linear retardation. At $T = 15°\mathrm{C}$, the retardation and its variation across the SOT field of view are significantly larger than our tolerance, as indicated by the contours. Such linear retardation may be created by lateral stress induced by the housing, since neither lenses nor housing are ideal owing to machining errors. It is also revealed that the behavior of the linear retardation has significant hysteresis. Figure 8 shows the history of the $[2, 4]$ element of the CLU Mueller matrix averaged over the SOT field of view versus temperature through various environmental tests.

After extensive measurements, we reached the following conclusions regarding the polarization of the CLU: The only significant polarization effect of the CLU is a linear retardation (*i.e.*, there are no linear and circular diattenuations, no circular retardation, and no depolarization). The CLU linear retardation may be regarded as uniform over the SOT field of view and constant against T at temperatures higher than 25°C. The CLU retardation can have a small, unpredictable shift following launch vibration and the initial cold cycle in orbit. The signature of circular to linear crosstalk will be checked after launch by using a simple sunspot, and that part of the calibration matrix will be updated if necessary. The lower limit of the operational temperature range of the CLU was thus set as 25°C, which will be maintained by the OTA operational heaters in orbit.

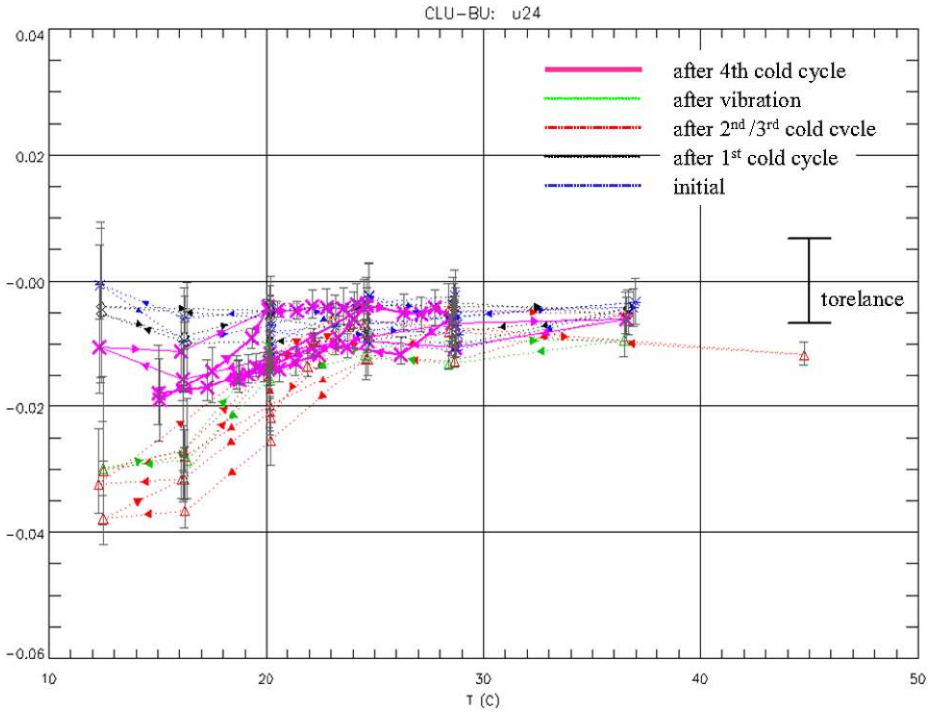

Figure 8 Hysteresis of (2, 4) element (= linear retardation) of the CLU Mueller matrix against temperature. The averages over the SOT FOV are plotted with error bars showing the variation across the SOT FOV.

5. System Calibration

5.1. Definition of Coordinate System

Figure 9 shows the definition of the polarization coordinate system of the SOT with respect to the spacecraft coordinates. This definition follows the standard convention used in the data analysis of the ASP (Advanced Stokes Polarimeter; Skumanich and Lites, 1997); that is, right circular polarization is positive when the electric vector rotates clockwise looking at the source, and positive V on the blue side of spectral lines gives positive magnetic flux. Note that this definition is applied to the Stokes vectors obtained after application of the **X** matrix; therefore, the raw Stokes products of the SOT (which are also called $IQUV$) are not consistent with this definition.

5.2. Test Setup and Measurements

Measurement of the polarimeter response matrix of the SOT was performed by using natural sunlight fed by a heliostat at the NAOJ clean room (see Figure 10). The entire SOT (with the OTA and the FPP attached to the spacecraft Optical Bench Unit) was located under the heliostat. Well-calibrated sheet polarizers (linear, left, and right circular) were placed at the entrance of the telescope at 0°, 45°, 90°, and 135°. The polarizers create the incident Stokes vectors. At each position of the sheet polarizer, data were taken by both the SP and the NFI in typical observing sequences, with multiple sets of polarization products corresponding to

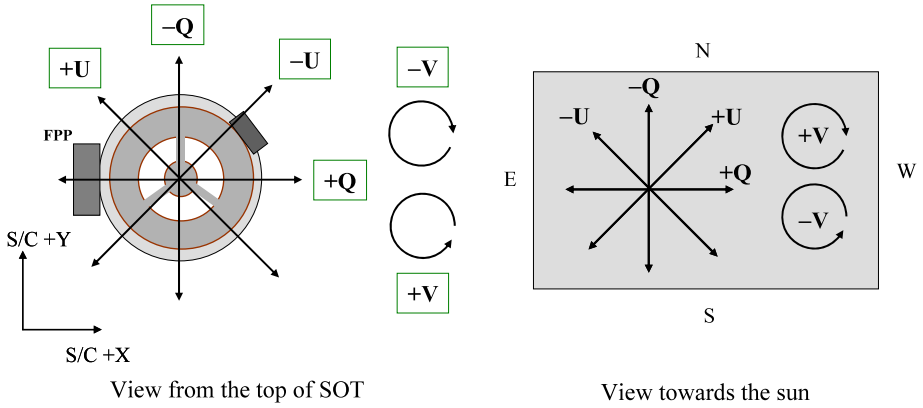

Figure 9 The definition of the SOT polarization coordinates.

Figure 10 Configuration of the SOT polarization calibration testing system.

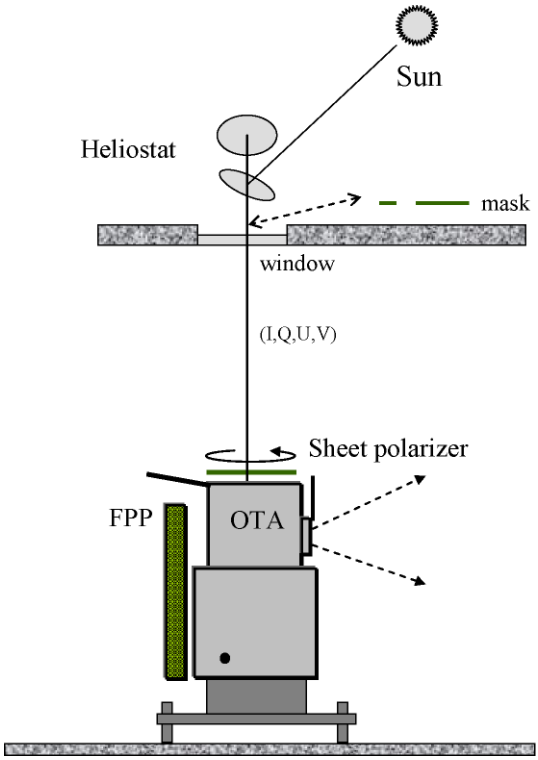

12 different incident Stokes vectors obtained. The data were taken for the entire slit scan range of the SP and at all available wavelengths using representative exposure schemes for the FG/NFI. During testing, the room temperature was controlled at 20°C, while the OTA operational heater was applied to maintain the CLU temperature at $T > 25$°C.

The sheet polarizers used for the test were HN38 (linear), HNCP37R (right-hand circular), and HNCP37L (left-hand circular), all provided by 3M Corporation. Their Mueller

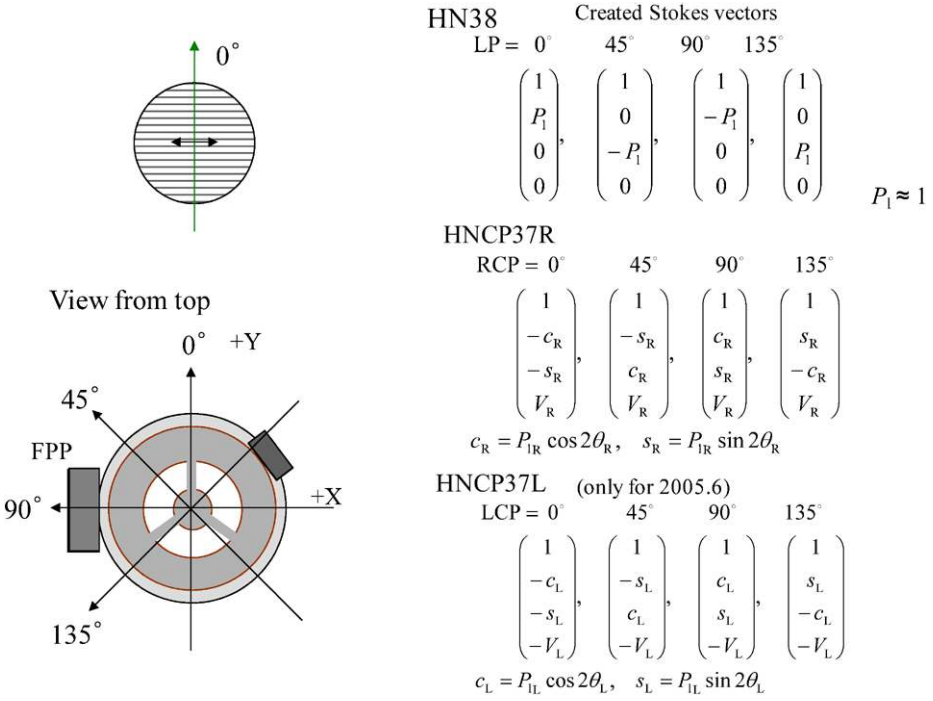

Figure 11 Configuration of sheet polarizer and incident Stokes vector.

matrices at 630 nm were obtained prior to testing by using the NAOJ Mueller matrix measurement system (Ichimoto *et al.*, 2006). The configurations of the sheet polarizer and corresponding incident Stokes vectors are shown in Figure 11. V_R and P_{lR} are circular and linear diattenuations of HNCP37R , and V_L and P_{lL} are circular and linear diattenuations of HNCP37L, respectively. We obtained values of $V_R = 0.9811$, $P_{lR} = 0.1496$, $V_L = 0.9905$, and $P_{lL} = 0.0637$ from the Mueller matrix measurements. The angles θ_R and θ_L are the orientations of the linear diattenuation of the HNCP37R and HNCP37L, respectively, and are regarded as unknown parameters in the following data reduction. It may be shown that the polarization produced by the heliostat ($< 5\%$) is negligible when these sheet polarizers are placed in front of the OTA.

Table 4 summarizes the data set taken during the two test periods for the SOT polarization calibration. The data sets marked with circles were used for the following analysis.

5.3. Derivation of the Polarimeter Response Matrix

The relation between the data products of the SP ($\mathbf{S}'$) and incident Stokes vectors ($\mathbf{S}$) may be written as follows:

$$\mathbf{S}'^{\pm}_k = \mathbf{X}^{\pm}\mathbf{T}\mathbf{S}_k \equiv \alpha^{\pm} I_k \mathbf{x}^{\pm}\mathbf{s}_k,$$

$$\begin{pmatrix} I'_k \\ Q'_k \\ U'_k \\ V'_k \end{pmatrix}^{\pm} = \alpha^{\pm} I_k \begin{bmatrix} 1 & x_{10} & x_{20} & x_{30} \\ x_{01} & x_{11} & x_{21} & x_{31} \\ x_{02} & x_{12} & x_{22} & x_{32} \\ x_{03} & x_{13} & x_{23} & x_{33} \end{bmatrix}^{\pm} \begin{pmatrix} 1 \\ q_k \\ u_k \\ v_k \end{pmatrix},$$

Table 4 List of data sets for the SOT polarization calibration.

λ	5172	5250	5896	6302	6563	Date	
FG shuttered $IQUV$							
(exp = 90 ms)							
2048 × 1024 (2 × 2sum, OBS_ID = 3)	–	○	○	○	○	2004.8.19/20	
512 × 1024 (2 × 2sum, OBS_ID = 3)	(○)	(○)	(○)	(○)	(○)	2005.6.13	Quality is poor (not used)
FG shutterless $IQUV$							
(exp = 100 ms)							
64 × 2048 (1 × 1sum, OBS_ID = 33)	–	○	○	○	○	2004.8.19/20	Mask = 82
80 × 1024 (2 × 2sum)	–	○	○	○	○	2004.8.19/20	Mask = 112
72 × 1024 (2 × 2sum)	○	○	○	○	○	2005.6.13/14	Mask = 112
SP							
224 × 1024 (1 × 1sum)				△		2004.8.19/20	SP opt. was modified later
				○		2005.6.13/14	

where $\mathbf{S}'_k$ is the SP product, $\mathbf{s}_k$ is the normalized incident Stokes vector with $I = 1$, $\pm$ stands for the left and right CCD areas (measuring orthogonal polarizations), and k stands for the configuration of the sheet polarizer. Each element of $\mathbf{X}$ is determined by a least-squares fitting procedure by using the normalized equation by each I'_k to eliminate the variability of the sky transmission,

$$\begin{pmatrix} Q'_k/I'_k \\ U'_k/I'_k \\ V'_k/I'_k \end{pmatrix} \equiv \begin{pmatrix} q'_k \\ u'_k \\ v'_k \end{pmatrix} = \frac{\begin{bmatrix} x_{01} & x_{11} & x_{21} & x_{31} \\ x_{02} & x_{12} & x_{22} & x_{32} \\ x_{03} & x_{13} & x_{23} & x_{33} \end{bmatrix}}{1 + x_{10}q_k + x_{20}u_k + x_{30}v_k} \begin{pmatrix} 1 \\ q_k \\ u_k \\ v_k \end{pmatrix}.$$

The number of equations is thus $3 \times 12 \times 2 = 72$, while the number of unknowns is 15×2 (with $x_{00} = 1$). Fitting is carried out for each pixel of the CCD, but θ_{R} and θ_{L} (the offset angles of RCP and LCP) are determined prior to the fitting from the average over the CCD.

A similar approach is applied to obtain the $\mathbf{X}$-matrix elements of the FG/NFI, but only for one CCD, and the degree of circular/linear polarization of the circular polarizers is also regarded as unknown since we do not have Mueller matrix measurements of them at wavelengths other than 630.2 nm. The values of θ_{R}, θ_{L}, P_{lR}, and P_{lL} (the offset angles and linear polarizations of RCP and LCP) are determined from the average over the CCD and then fixed in fitting for each pixel by assuming $P^2_{\mathrm{cR}} + P^2_{\mathrm{lR}} = 1$ and $P^2_{\mathrm{cL}} + P^2_{\mathrm{lL}} = 1$. Thus, the number of unknowns is 15 and the number of equations is $3 \times 12 = 36$.

Thus the $\mathbf{X}$-matrix elements were determined as a function of the position in the FOV. We obtained two-dimensional maps of polarimeter response matrices for the SP at multiple scan positions covering its entire range and for the NFI in all available wavelengths for representative exposure schemes.

5.4. SP Polarimeter Response Matrix

It should be noted that the analyses of the SOT/SP polarization calibration measurements were carried out completely independently by two separate methods (at HAO and NAOJ). These methods produced the same results within the measurement error. The HAO calibration scheme has a heritage from calibration of the Advanced Stokes Polarimeter (Skumanich and Lites, 1997). It has been used to calibrate other ground-based polarimeters. Here we present results derived from the NAOJ scheme, but the calibration software for flight data currently utilizes data resulting from the HAO calibration.

Figure 12 shows an example of observed products of the SP along with fitting results for both left and right CCD areas. This result is for a particular pixel at the center of the CCD and for the center of the slit scan range. The fitting is satisfactory and each element of the **X** matrix is well determined. Figure 13 shows the two-dimensional distribution of **X** over the CCD at the scan center. Representative matrices for the left and right CCDs consisting of the median values of each element are also shown. Figure 14 shows **X**-matrix elements (median value in the CCD) as a function of the scan position. The horizontal dotted lines show the tolerance of each element defined in Section 2. From both Figures 13 and 14, we may regard the **X** matrix as uniform over both the CCD and the scan range (*i.e.*, within the tolerance defined in Section 3). There is, however, a systematic trend in some elements with the scan position or position in the CCD, which may be corrected in data reduction.

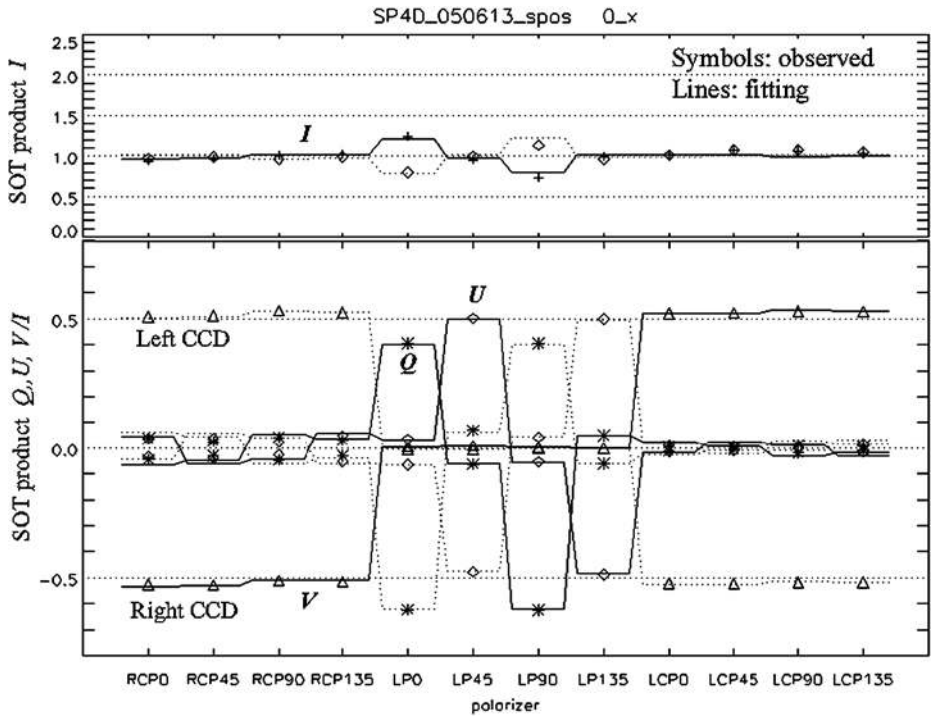

Figure 12 The observed SP products for 12 different configurations of the sheet polarizer (symbols) and results of the least-squares fitting (lines). The left and right CCDs are shown by solid and dotted lines, respectively.

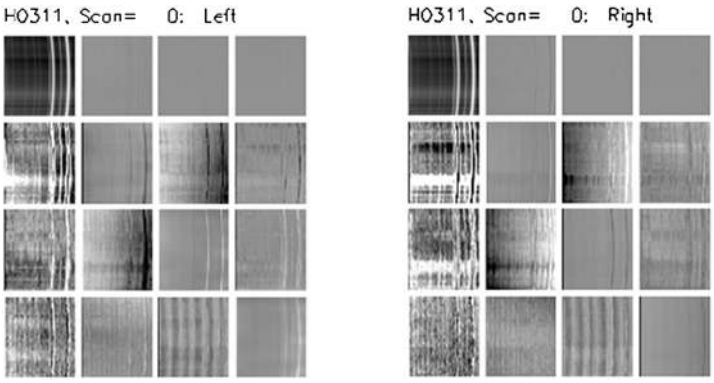

Figure 13 **X**-matrix spatial distribution over the CCD. Each element is scaled to median $\pm$ tolerance, and x_{00} $(=1)$ is replaced by the I image.

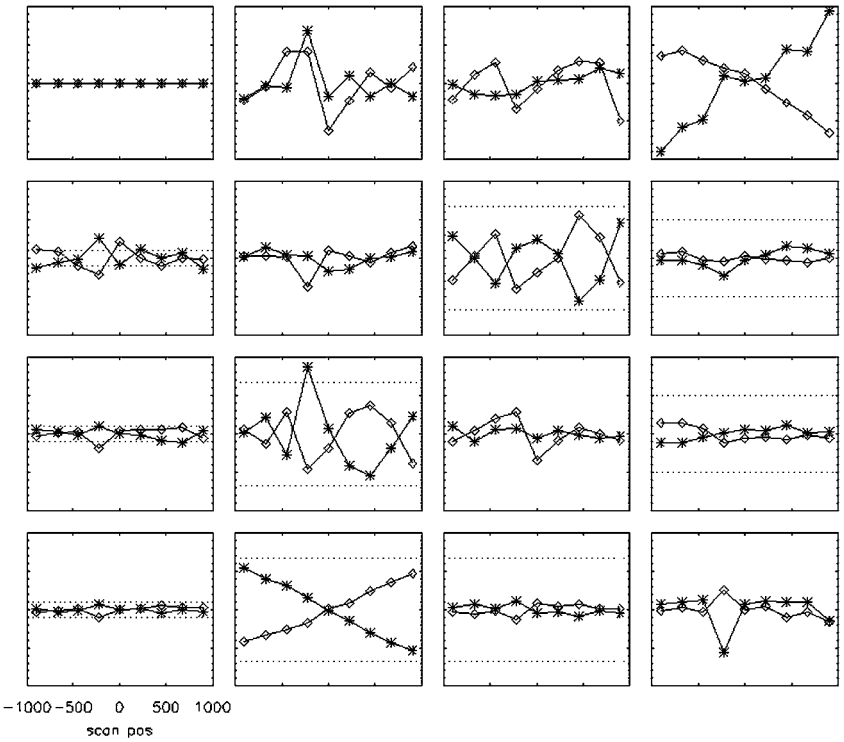

Figure 14 **X**-matrix elements (median value in CCD) as a function of scan position. Left and right CCD areas are shown by diamonds and asterisks, respectively. The horizontal dotted lines indicate the tolerance of each element as defined in Section 3.

5.5. NFI Polarimeter Response Matrix

Figure 15 shows examples of the observed products and results of the least-squares fitting for the NFI at 630.2 and 525.0 nm at the center of the CCD in the same manner as just demonstrated for the SP. The fitting is again successful, and the 15 elements of the response matrix are well determined for each CCD pixel. Figure 16 shows the spatial distribution of the **X** matrix over the CCD in NFI shuttered mode at 630.2 nm. The FOV covers the entire CCD, but the very left and right edges were obscured by an improper optical baffle during this test period in 2004. The plot in the right panel shows the horizontal cross sections of each element (with all rows overplotted). These plots again demonstrate that the **X** matrix may be regarded as uniform over the CCD. Figure 17 shows the spatial distribution of the **X** matrix over the CCD in NFI shutterless mode at 630.2 nm. The FOV covers a central 160×2048 pixel region. Note in the right-panel plot that the $(2, 3)$ and $(3, 2)$ elements show a discrete jump at the center of the FOV with an amount exceeding our tolerance. This behavior is due to the successive readout scheme of the CCD; the left half is read first and then the right half is read, and there is a time delay in effective exposure between left and right halves by about 2.83 ms. This jump corresponds to the mutual rotation of the $Q-U$ frame or rotation of the B azimuth between the two halves of the CCD by 2.83°. This effect will be corrected by the calibration. In each half of the CCD, the **X** matrix may be regarded as uniform. The experimental polarimeter response matrices were obtained for all wavelengths in which the NFI performs polarization measurements, namely, for 517.2, 525.0, 589.6, 630.2, and 656.3 nm.

5.6. Repeatability of the Measurement

To confirm the reliability of the measurements, we repeated the same measurement on different days during the test periods and checked the repeatability of the results. The following matrices show the difference of the SP **X** matrices (median for each left and right CCD) on two successive days (2005.6.13 and 6.14) as an example:

Left				Right			
0.0000	−0.0041	−0.0032	−0.0008	0.0000	0.0368	0.0018	−0.0032
−0.0023	−0.0093	0.0021	0.0007	0.0094	0.0079	0.0048	−0.0069
−0.0014	0.0040	−0.0071	−0.0008	0.0004	−0.0037	0.0099	−0.0000
−0.0012	0.0002	0.0001	0.0066	0.0005	0.0006	−0.0014	−0.0053

The differences shown without underlining are within our tolerance, and we conclude that the accuracy of the measurement is good enough for most **X**-matrix elements except for the first column. Elements in the first column will be determined in orbit by using the continuum in the solar spectrum. This is also the case for the NFI.

6. Modeling of the SOT Polarization

We have successfully determined the experimental polarimeter response matrices for typical NFI observing sequences, but the NFI has a variety of exposure schemes with a variety of exposures, on-chip summing, and polarization sampling. Furthermore, new exposure schemes can be added after the launch whenever they are demanded. We do not have experimental **X**-matrix measurements for each case. To extend our knowledge of the **X** matrices of the

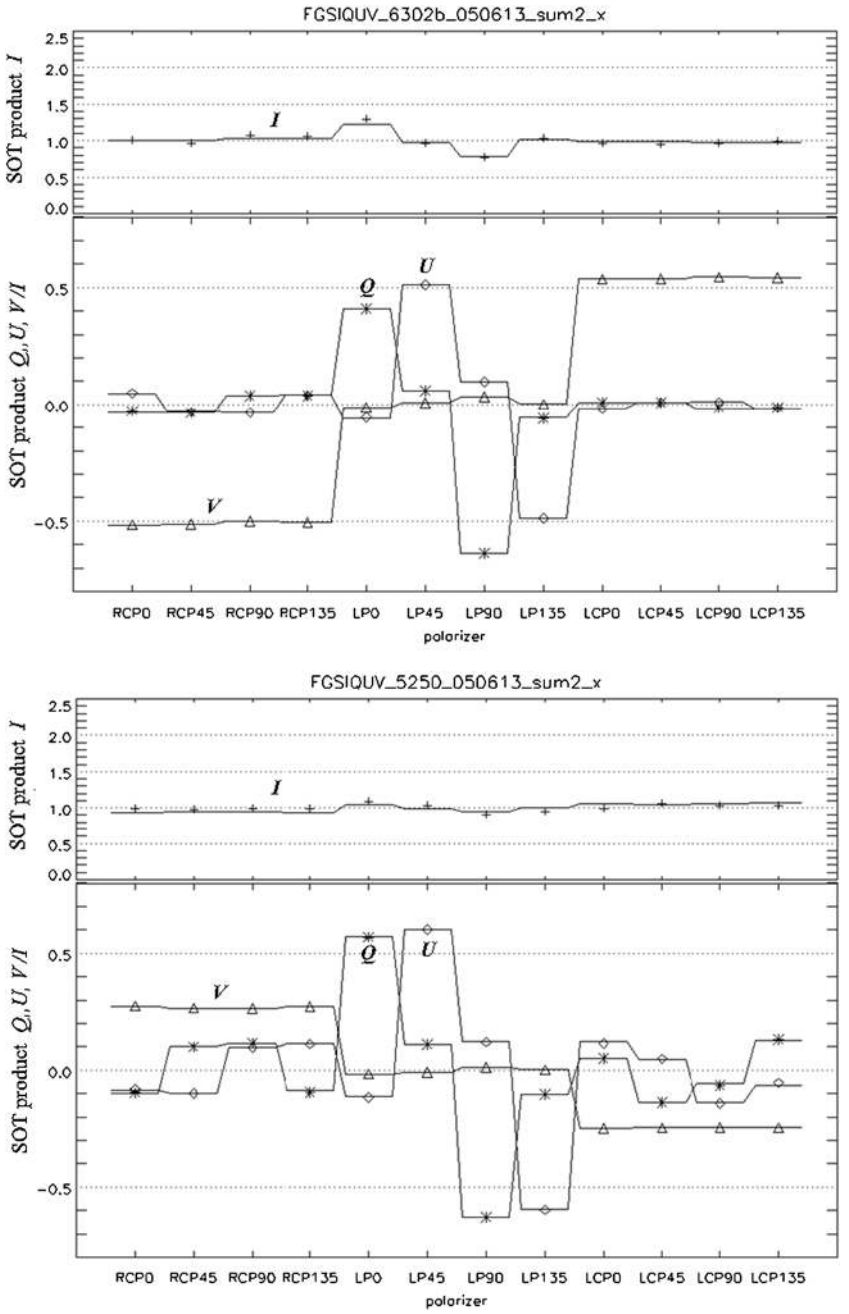

Figure 15 Same as Figure 12 but for the NFI at 630.2 nm (top) and 525.0 nm (bottom).

tested cases, a simple "SOT polarization model" is created, from which we may predict the **X** matrix for arbitrary observing sequences. There is another need for the SOT polarization model. Since, during the polarization calibration test, the entire FOV is illuminated by

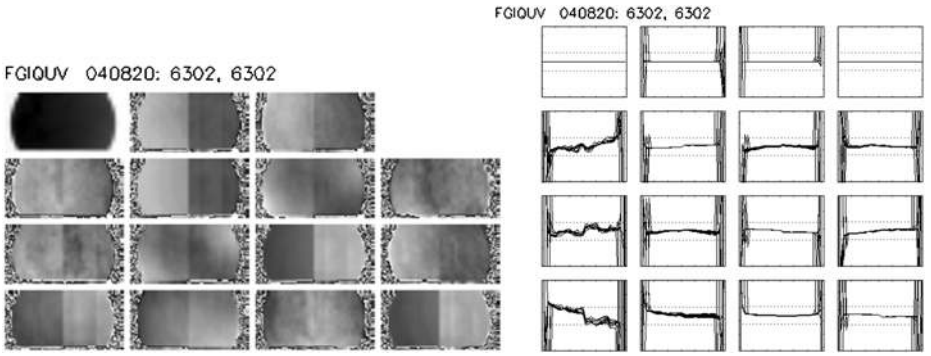

Figure 16 **X** matrix in NFI shuttered mode at 630.2 nm. Two-dimensional image over the CCD (left) and their plots against the y-coordinate (right). In the right panel, horizontal dotted lines show the tolerance of each element.

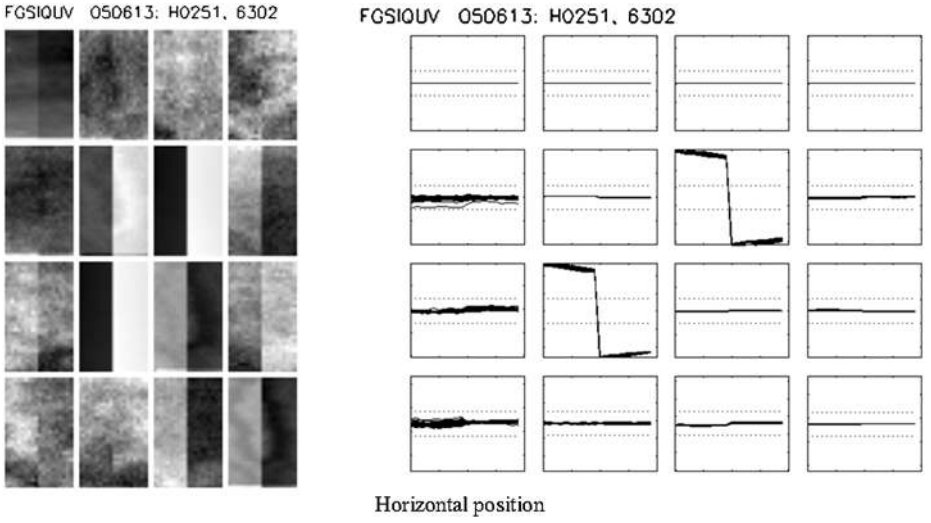

Figure 17 **X** matrix in NFI shutterless mode at 630.2 nm. Two-dimensional image over the CCD (left) and their plots against the y-coordinate (right). In the right panel, horizontal dotted lines show the tolerance of each element. The FOV covers the central 160 × 2048 pixels with 2 by 2 summing.

uniformly polarized light, some experimental **X**-matrix elements in shutterless mode have a variation across the FOV as the result of "polarization smearing" (see Section 6.2). Our SOT polarization model incorporates the correction of this artificial effect in experimental **X** matrices.

6.1. Basic Formulations

The assumptions of this model are as follows:

- The PMU is an ideal retarder and the polarization analyzer is an ideal linear polarizer.
- Exposure time and intervals between successive exposures are per flight software specifications.

- Any deviations of **X** from the theoretical matrix are attributed to the telescope matrix described in the following.
- The **X** matrix is uniform over each area (left and right) of the CCD.

The SOT data product, $\mathbf{S}_{\mathrm{SOT}}$, and the polarimeter response matrix, **X**, may be expressed as

$$\mathbf{S}_{\mathrm{SOT}} = \mathbf{X}\mathbf{S}_{\mathrm{in}} = \mathbf{DWTS}_{\mathrm{in}},$$

or

$$\mathbf{X} = \mathbf{DWT},$$

where **D** is the demodulation matrix ($N \times 4$ elements, with N the number of exposures),

$$\mathbf{W} = (1, 1, 0, 0)\mathbf{P}(\delta_\lambda, \phi_k, \Delta t)$$

is the polarization measurement matrix ($4 \times N$ elements with $k = 0, \ldots, N-1$ standing for the sequence number of exposure), and **T** is the telescope Mueller matrix, with $(1, 1, 0, 0)$ as the first row of a Mueller matrix for an ideal analyzer and $\mathbf{P}(\delta, \phi_k, \Delta t)$ as the PMU matrix under continuous rotation, $k = 0, \ldots, N-1$, given by

$$\begin{aligned}\mathbf{P}(\delta_\lambda, \phi_k, \Delta t) &= \int_{\phi_1}^{\phi_2} \mathbf{R}(-\phi)\mathbf{M}_{\mathrm{ret}}(\delta_\lambda)\mathbf{R}(\phi)\,\mathrm{d}\phi \\ &= \begin{pmatrix} \Delta\phi & 0 & 0 & 0 \\ 0 & c_2 + s_2\cos\delta & (1-\cos\delta)d & -s_1\sin\delta \\ 0 & (1-\cos\delta)d & c_2\cos\delta + s_2 & c_1\sin\delta \\ 0 & s_1\sin\delta & -c_1\sin\delta & \Delta\phi\cos\delta \end{pmatrix}_k\end{aligned}$$

where

$$c_1 \equiv \int_{\phi_1}^{\phi_2} \cos 2\phi\,\mathrm{d}\phi = \left[\frac{1}{2}\sin 2\phi\right]_{\phi_1}^{\phi_2}, \qquad c_2 \equiv \int_{\phi_1}^{\phi_2} \cos^2 2\phi\,\mathrm{d}\phi = \left[\frac{\phi}{2} + \frac{1}{8}\sin 4\phi\right]_{\phi_1}^{\phi_2},$$

$$s_1 \equiv \int_{\phi_1}^{\phi_2} \sin 2\phi\,\mathrm{d}\phi = \left[-\frac{1}{2}\cos 2\phi\right]_{\phi_1}^{\phi_2}, \qquad s_2 \equiv \int_{\phi_1}^{\phi_2} \sin^2 2\phi\,\mathrm{d}\phi = \left[\frac{\phi}{2} - \frac{1}{8}\sin 4\phi\right]_{\phi_1}^{\phi_2},$$

$$d \equiv \int_{\phi_1}^{\phi_2} \cos 2\phi \sin 2\phi\,\mathrm{d}\phi = \left[-\frac{1}{4}\cos^2 2\phi\right]_{\phi_1}^{\phi_2}, \qquad \Delta\phi \equiv \phi_2 - \phi_1 = \omega \cdot \Delta t,$$

with

$$\begin{aligned}\phi_1 &= \phi_k - \omega \cdot \Delta t/2, \\ \phi_2 &= \phi_k + \omega \cdot \Delta t/2, \\ \omega &= 2\pi/1.6\ \mathrm{rad\,s^{-1}},\end{aligned}$$

and where ϕ_k is the phase angles of the PMU at the center of each exposure, Δt is the exposure time, δ_λ is the retardation of the waveplate, and λ is the wavelength.

Using the response matrices obtained by the experiments, $\mathbf{X}_{\mathrm{ex}}$, we performed a least-squares fitting for **X** with dt (exposure delay time) and δ_λ (retardation) as unknowns,

$$\mathbf{X}_{\mathrm{ex}} \approx \mathbf{X}_{\mathrm{fit}} = \mathbf{DW}(\phi_k, \Delta t, \mathrm{d}t, \delta_\lambda)$$

with ϕ_k and Δt fixed to the specified values. The telescope matrix is determined by

$$\mathbf{T}(\lambda) = \mathbf{X}_{\rm fit}^{-1}\mathbf{X}_{\rm ex}$$

for each experimental data set. Then $\mathbf{T}(\lambda)$ and δ_λ are averaged over data sets for the same wavelength. The time delay dt is averaged for each left and right half of the CCD of the shuttered and shutterless modes. Thus the SOT polarization model provides the $\mathbf{X}$ matrix for arbitrary sequence specified by ϕ_k and Δt by

$$\mathbf{X}_{\rm model} = \mathbf{DW}\left(\phi_k, \Delta t, \overline{\delta}_\lambda, \overline{{\rm d}t}\right)\overline{\mathbf{T}}_\lambda.$$

6.2. Correction for Polarization Smearing

Each pixel in the SP and in the FG shutterless mode experiences smearing periods during the frame transfer, The mean PMU phase angle in an exposure (or effective exposure timing) differs with the position of the pixel on the CCD. Since the incident light is uniformly polarized in the FOV in the polarization calibration test, the variation of effective timing along the CCD appears as the slope of (2, 3) and (3, 2) elements of the derived response matrix along the CCD x-coordinate (see Figures 13 and 17). This is not the case for a real observation of the highly structured Sun. To eliminate this artificial effect in the experimental $\mathbf{X}$, we need to apply an additional correction to the SOT polarization model.

Figure 18 shows a chart describing the "exposure" sequence in NFI shutterless mode. In the chart, $t_{\rm p}$ is the center of the illuminated period ($\Delta t_0 + \Delta t_1 + \Delta t_2$) whose timing is determined from the fitting of the experimental $\mathbf{X}$ matrix (dt). As inferred from the chart, this timing depends on the mask size and pixel position on the CCD. The parameter $t_{\rm c}$ is the center of the exposure cycles, which does not depend on either the mask size or pixel position.

The SOT data product is a summation of contributions from three periods – Δt_0, Δt_1, and Δt_2 – where Δt_0 is the period for charge being transferred from the CCD center to the pixel position $x_{\rm p}$, Δt_1 is the period of the exposure at the pixel position, and Δt_2 is the period

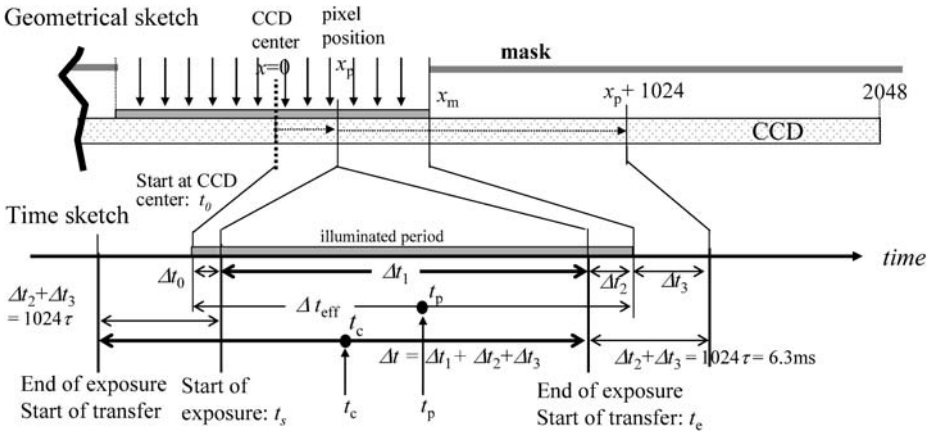

Figure 18 Geometrical and temporal sketch of exposure timing for the shutterless mode. Δt is the "exposure" time (typically = 100 ms); Δt_1 is the exposure at the pixel position; and Δt_0, Δt_2 is the smearing period.

for the charge being transferred from the pixel position x_p to the mask edge. Thus the SOT product is

$$\mathbf{S}_{\rm SOT} = \mathbf{D}\big[\mathbf{W}(\Delta t_0)\mathbf{T}\,\mathbf{S}_{\rm in0} + \mathbf{W}(\Delta t_1)\mathbf{T}\,\mathbf{S}_{\rm in1} + \mathbf{W}(\Delta t_2)\mathbf{T}\,\mathbf{S}_{\rm in2}\big].$$

In the polarization calibration test where the polarization is uniform over the SOT FOV,

$$\mathbf{S}_{\rm in0} = \mathbf{S}_{\rm in2} = \mathbf{S}_{\rm in1},$$

and thus

$$\mathbf{S}_{\rm SOT} = \mathbf{D}\big[\mathbf{W}(\Delta t_0) + \mathbf{W}(\Delta t_1) + \mathbf{W}(\Delta t_2)\big]\mathbf{T}\mathbf{S}_{\rm in1}$$

and

$$\mathbf{X}_{\rm ex} = \mathbf{X}(\Delta t_0) + \mathbf{X}(\Delta t_1) + \mathbf{X}(\Delta t_2).$$

In real solar observations, in contrast, since the smear regions (exposed areas during Δt_0 and Δt_2) are likely to have mixed polarity, $Q, U, V = 0$ on average and

$$\mathbf{S}_{\rm in0} = \mathbf{S}_{\rm in2} = (I, 0, 0, 0)^{\rm T}.$$

Then

$$\mathbf{S}_{\rm SOT} = (\Delta I, 0, 0, 0)^{\rm T} + \mathbf{D}\mathbf{W}(\Delta t_1)\mathbf{T}\mathbf{S}_{\rm in1} = (\Delta I, 0, 0, 0)^{\rm T} + \mathbf{X}(\Delta t_1)\mathbf{S}_{\rm in1},$$

where $\Delta I = I(\Delta t_0 + \Delta t_2)/(\Delta t_0 + \Delta t_1 + \Delta t_2)$ is the bias intensity resulting from smearing (with $\mathbf{T} \approx 1$ assumed). Since our aim is to obtain $\mathbf{S}_{\rm in1}$ for a real observation,

$$\mathbf{S}_{\rm in1} = \mathbf{X}(\Delta t_1)^{-1}\big[\mathbf{S}_{\rm SOT} - (\Delta I, 0, 0, 0)^{\rm T}\big], \quad \mathbf{X}(\Delta t_1) = \mathbf{D}\mathbf{W}(\Delta t_1)\mathbf{T}.$$

$\mathbf{X}(\Delta t_1)$ is the polarization calibration goal in NFI shutterless mode. As inferred from Figure 18, $\mathbf{X}_{\rm ex}$ depends on both mask size and pixel position on the CCD, but $\mathbf{X}(\Delta t_1)$ is independent of both mask size and pixel position.

The target matrix $\mathbf{X}(\Delta t_1)$ may then be calculated by the following equation:

$$\mathbf{X}(\Delta t_1) = \int_{t_{\rm s}}^{t_{\rm e}} \mathbf{X}(t)\,{\rm d}t = \int_{t_{\rm c}-\Delta t/2+1024\tau}^{t_{\rm c}+\Delta t/2} \mathbf{X}(t)\,{\rm d}t,$$

where $t_{\rm c}$ (the center of the exposure cycle, which is independent of the pixel position and the mask) is converted from $t_{\rm p}$ by

$$t_{\rm c} = t_{\rm p} - \tau(512 + x_{\rm m}/2 - x_{\rm p}),$$

with $\tau = 0.00615$ ms/pixel being the rate of frame transfer. Using this formula, one can correct the exposure delay time dt in the polarization model.

6.3. Results from the SOT Polarization Model

Table 5 summarizes the parameters obtained for the SOT polarization model for each wavelength. The integer part of the retardation of the PMU is that specified in the design of the waveplate. Notice that the modulation amplitudes for both linear and circular polarization

Table 5 Parameters of the SOT polarization model.

Wavelength (nm)	Retardation (waves)		Modulation amplitude (diagonal element of X in shutterless mode)		Time delay of t_c (ms)			
					Shutterless		Shuttered	
	Design	Measured	QU	V	Left	Right	Left	Right
517.3	6.650	6.6822	0.45	0.58	−0.24	6.16	–	–
525.0	6.558	6.5720	0.61	0.27	0.80	7.09	−5.52	−5.55
589.6	5.816	5.7624	0.30	0.63	0.28	6.63	−5.47	−6.05
630.2	5.350	5.3442	0.50	0.53	−1.47	4.93	−7.99	−7.52
656.3	5.050	5.1095	0.07	0.40	−4.23	3.02	−9.87	−9.35

Note. There is no measurement of the time delay in the shuttered mode at 517.3 nm. In the reduction of flight data, the same delay at 525.0 nm will be assumed.

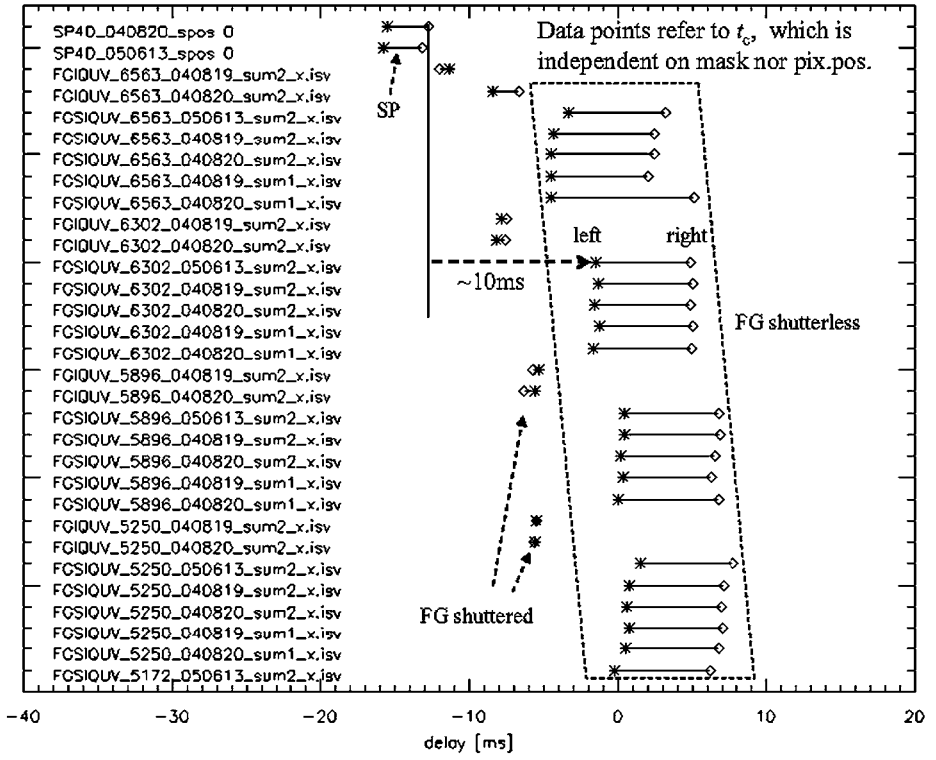

Figure 19 Time delay of exposure in all data sets. Asterisks and diamonds refer to the left half and right half, respectively, of the CCD.

are equivalent at 517.3 and 630.2 nm (as intended by the design) and high modulation efficiency for circular polarization at 589.6 nm, high modulation efficiency for linear polarization at 525.0 nm, and less modulation efficiency for linear polarization in Hα are realized. In Figure 19, a plot of time delay (effective exposure timing) for all data sets used in the analysis is shown. There is an obvious dependence of the delay on wavelength, the cause of

Table 6 Telescope matrices and the standard deviation of the fitting residual with the SOT polarization model.

Average T matrix					STD deviation of fitting residual			
6563	0.9893	−0.0420	−0.0491	0.0018	0.0000	0.0117	0.0296	0.0113
	−0.0121	−0.9541	0.0190	0.0072	0.0006	0.0025	0.0005	0.0009
	−0.0052	0.0088	0.9764	0.0205	0.0010	0.0011	0.0015	0.0013
	−0.0049	−0.0285	−0.0135	1.0070	0.0008	0.0010	0.0019	0.0067
6303	0.9976	0.0101	0.0276	0.0031	0.0000	0.0069	0.0087	0.0062
	0.0108	0.9990	0.0145	−0.0025	*0.0028*	0.0080	0.0022	0.0036
	0.0030	0.0131	0.9983	−0.0157	*0.0012*	0.0021	0.0079	0.0017
	−0.0050	0.0437	0.0099	0.9763	*0.0015*	0.0020	0.0010	0.0086
5896	0.9951	0.0008	0.0730	−0.0006	0.0000	0.0075	0.0107	0.0028
	0.0091	0.9970	0.0144	−0.0010	*0.0018*	0.0046	0.0018	0.0013
	0.0013	0.0147	1.0021	−0.0143	*0.0018*	0.0016	0.0049	0.0019
	−0.0099	−0.0178	0.0111	0.9927	0.0010	0.0031	0.0009	0.0103
5250	0.9994	0.0061	0.0141	−0.0082	0.0000	0.0040	0.0148	0.0199
	0.0113	0.9996	0.0131	0.0011	*0.0032*	0.0083	0.0046	0.0027
	0.0030	0.0136	1.0031	−0.0169	*0.0043*	0.0033	0.0137	0.0042
	−0.0169	−0.0459	0.0025	0.9931	*0.0011*	0.0015	0.0020	0.0074
5172	0.9998	0.0007	−0.0296	−0.0458	–	–	–	–
	−0.0007	1.0003	0.0077	−0.0077	–	–	–	–
	−0.0018	0.0093	0.9863	0.0149	–	–	–	–
	−0.0139	0.0543	−0.0246	0.9901	–	–	–	–

Note. Elements in italics exceed the tolerance. Standard deviations are not given for 5172 Å since we have only a single measurement for this wavelength.

which is not well understood but is likely due to fabrication error of the waveplate. Residuals of the fitting (*i.e.*, the difference of $\mathbf{X}_{\rm ex}$ and $\mathbf{X}_{\rm fit} = \mathbf{DW}$) averaged in each wavelength for the telescope matrices are shown in Table 6. The standard deviations of the fitting residual are also shown in the right side of Table 6. Since all elements of the standard deviation other than the first column are smaller than the tolerances of the response matrix, we can consider that the SOT polarization model developed here well represents the real polarization response matrix of the NFI except for the first column. The elements of the first column will be determined in orbit, again by using continuum values.

For reference, the polarimeter response matrices provided by the SOT polarization model are presented in Table 7 for the NFI shutterless *IQUV* mode, where the telescope matrix is assumed to be unity.

7. Examples of Extended Observing Schemes for the NFI

7.1. Magnetogram (IV Mode)

So far we have been focusing on observations of full Stokes parameters in which a 4×4 polarimeter response matrix is applicable to retrieve the incident Stokes vector. The NFI can

Table 7 The polarimeter response matrices provided by the SOT polarization model for the NFI shutterless *IQUV* mode (Obs_ID = 33, exposure = 100 ms). The telescope matrix is assumed to be unity.

	Left-CCD				Right-CCD			
6563	1.0000	0.8863	0.0000	0.0000	1.0000	0.8863	0.0000	0.0000
	0.0000	0.0723	0.0048	0.0000	0.0000	0.0723	−0.0034	0.0000
	0.0000	0.0048	−0.0723	0.0000	0.0000	−0.0034	−0.0723	0.0000
	0.0000	0.0000	0.0000	−0.4040	0.0000	0.0000	0.0000	−0.4041
6303	1.0000	0.2210	0.0000	0.0000	1.0000	0.2210	0.0000	0.0000
	0.0000	0.4958	0.0114	0.0000	0.0000	0.4944	−0.0384	0.0000
	0.0000	0.0114	−0.4958	0.0000	0.0000	−0.0384	−0.4944	0.0000
	0.0000	0.0000	0.0000	−0.5279	0.0000	0.0000	0.0000	−0.5279
5896	1.0000	0.5389	0.0000	0.0000	1.0000	0.5389	0.0000	0.0000
	0.0000	0.2935	−0.0013	0.0000	0.0000	0.2919	−0.0305	0.0000
	0.0000	−0.0013	−0.2935	0.0000	0.0000	−0.0305	−0.2919	0.0000
	0.0000	0.0000	0.0000	0.6374	0.0000	0.0000	0.0000	0.6338
5250	1.0000	0.0503	0.0000	0.0000	1.0000	0.0503	0.0000	0.0000
	0.0000	0.6046	−0.0076	0.0000	0.0000	0.6009	−0.0672	0.0000
	0.0000	−0.0076	−0.6046	0.0000	0.0000	−0.0671	−0.6009	0.0000
	0.0000	0.0000	0.0000	0.2783	0.0000	0.0000	0.0000	0.2778
5172	1.0000	0.2934	0.0000	0.0000	1.0000	0.2934	0.0000	0.0000
	0.0000	0.4498	0.0017	0.0000	0.0000	0.4477	−0.0434	0.0000
	0.0000	0.0017	−0.4498	0.0000	0.0000	−0.0434	−0.4477	0.0000
	0.0000	0.0000	0.0000	0.5797	0.0000	0.0000	0.0000	0.5790

also take IV information only with two exposures centered at the PMU phases at $\pm 45°$ (Figure 20) and the exposure time is selectable in shuttered mode. In practice such a mode, called a "magnetogram," is useful for making context longitudinal magnetograms at high cadence.

Intensities obtained by the two exposures are given by

$$I_+ = I + c_Q Q + c_V V,$$
$$I_- = I + c_Q Q - c_V V$$

and the polarimeter response matrix in this case consists of 4×2 elements,

$$\begin{pmatrix} I' \\ V' \end{pmatrix} = \begin{pmatrix} x_{00} & x_{10} & x_{20} & x_{30} \\ x_{03} & x_{13} & x_{23} & x_{33} \end{pmatrix} \begin{pmatrix} I \\ Q \\ U \\ V \end{pmatrix} \approx \begin{pmatrix} 1 & c_Q & 0 & 0 \\ 0 & 0 & 0 & c_V \end{pmatrix} \begin{pmatrix} I \\ Q \\ U \\ V \end{pmatrix}.$$

Here c_Q and c_V represent $Q \rightarrow I$ crosstalk and the efficiency of the V measurement, respectively, and are functions of exposure time. Figure 21 shows the plots of c_Q and c_V against the exposure time predicted from the SOT polarization model for five NFI wavelengths. The verification test of such curves was performed by using the FPP and backup

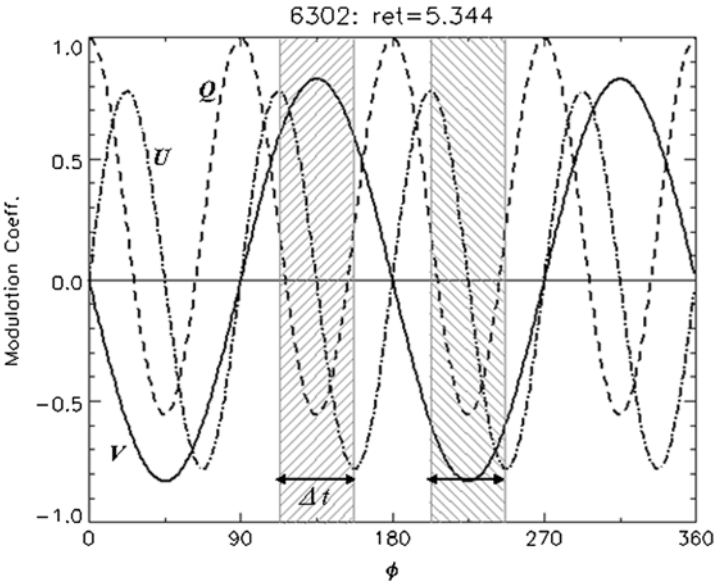

Figure 20 Exposure timing with respect to the PMU modulation phase for the NFI IV mode.

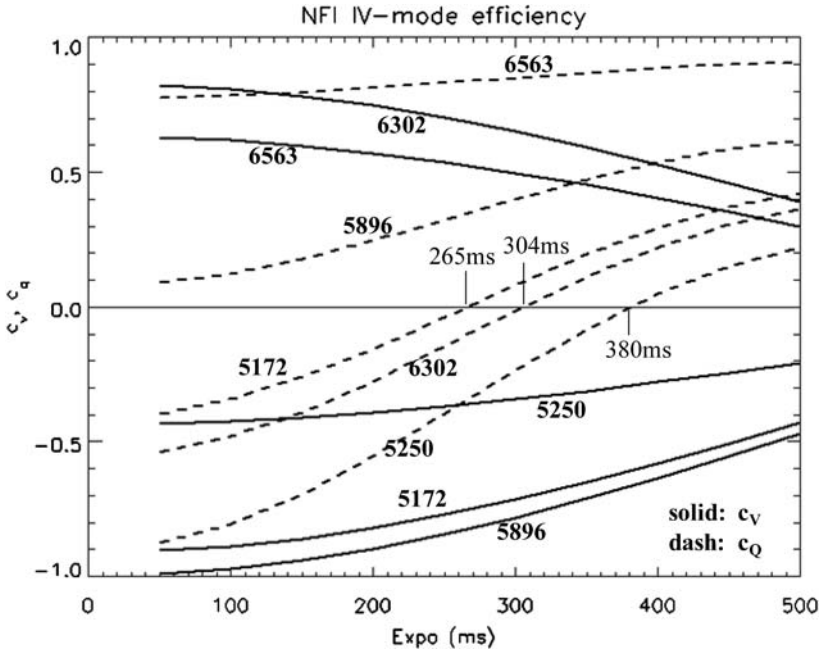

Figure 21 Plots of c_Q and c_V against the exposure time predicted from the SOT polarization model. Solid curves are c_V (efficiency of V measurement) and dashed curves are c_Q ($Q \rightarrow I$ crosstalk).

(flight spare) unit of the PMU. Figure 21 suggests that there is a preferable exposure time at which the $Q \rightarrow I$ crosstalk becomes negligible for each wavelength.

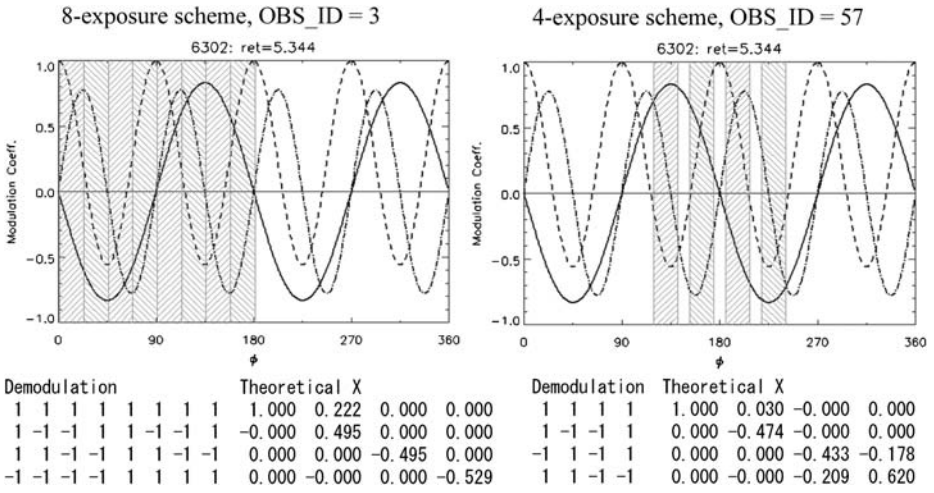

Figure 22 Eight-exposure scheme and four-exposure scheme of the NFI to get $IQUV$.

7.2. NFI Four-Exposure $IQUV$ Mode

In addition to the eight-exposure scheme to take $IQUV$, the FG shuttered mode has a four-exposure scheme whose **X** matrix was not measured with the real SOT. Figure 22 shows the exposure timing with respect to the PMU modulation curve for both schemes together with the theoretical polarimeter response matrices. The four-exposure scheme takes four exposures with equally spaced PMU phase angles centered at 180°. In our case the space is set as 33.1° with which we can maximize the modulation efficiency for V and equalize the modulation efficiencies for Q and U. The verification test of this scheme was again performed by using the FPP and PMU flight spare unit at 630.2 and 517.2 nm, and we have confirmed that the SOT polarization model well predicts the polarimeter response matrix of the four-exposure scheme.

8. Summary

Polarimeter response matrices of the SOT were determined experimentally by using the entire SOT for the SP and typical NFI observing modes as functions of position in the FOV. Matrix elements are determined to sufficient accuracy so that crosstalk among different Stokes parameters is suppressed below the typical statistical noise of 10^{-3}. The accuracy of measurements inferred from repeatability meets the required accuracy except for the first column of the matrices. The polarimeter response matrices can be regarded as uniform over the field of view except for the NFI shutterless mode, in which the left and right halves of the CCD have a non-negligible difference owing to the relative exposure delay between the two halves. Even though the variation of **X** for the SP is also smaller than the tolerance, we detected a smooth variation of the **X** matrix of the SP across its field of view, which is taken into account for calibration of flight data. The SOT polarization model reproduces experimental **X** matrices of the NFI with the required accuracy and can be used to predict the **X** matrices of other observing sequences for which the experimental **X** matrices were not obtained. The SOT polarization characteristics are expected to be fairly stable in orbit,

whereas the linear retardation of the CLU may have a small offset created during the launch load environment. This possible offset may be checked in real solar data and the **X** matrix will be updated if necessary.

Following the successful launch of *Hinode* on 22 September 2006, the SOT achieved its first light soon after the deployment of the top door of the telescope on 25 October. After the initial instrument checkout, the SP and the FG began making regular observations of the Sun and are producing excellent Stokes data. We have noticed that the three elements of the first column of **X** matrices are very close to zero from the SP and the FG/NFI continuum data. However, we have not yet found any sign implying an offset of the CLU linear retardation ($V \rightarrow QU$ crosstalk). We need to await further detailed analysis of sunspot data to finalize this issue.

Polarization calibrations of the SP data are being performed successfully on a regular basis by using the polarimeter response matrices obtained by HAO. An IDL procedure (fg_pcalx.pro) that provides polarization response matrices for arbitrary NFI products is ready and catalogued in the Solar Software (SSW) package.

Acknowledgements The authors are grateful to the late professor T. Kosugi of JAXA/ISAS and to Drs. L. Hill, R. Jayroe, and J. Owens of NASA for continuous support throughout the development of the SOT. The authors also thank Messrs. T. Matsushita and H. Saito of Mitsubishi Electric Corporation and Mr. N. Takeyama of Genesia Corporation for extensive thermomechanical analysis of the CLU and also Messrs. S. Abe and M. Suzuki of Canon Corporation for indispensable support for the polarization testing of the CLU. One of the authors (KI) also would like to thank Dr. E. West of Marshall Space Flight Center, Dr. R. Chipman of Alabama University, and Dr. Y. Otani of Tokyo University of Agriculture and Technology for valuable discussions on the polarization measurements of optical devices in the early phase of the project. *Hinode* is a Japanese mission developed and launched by ISAS/JAXA, with NAOJ as domestic partner and NASA and STFC (UK) as international partners. It is operated by these agencies in cooperation with ESA and NSC (Norway).

References

Elmore, D.F.: 1990, *A polarization calibration technique for the advanced stokes polarimeter*. *NCAR Technical Note NCAR/TN-355+STR*, NCAR, Boulder, Colorado.

Guimond, S., Elmore, D.: 2004, *OE Mag.* **4**(5), 26.

Ichimoto, K., Tsuneta, S., Suematsu, Y., Shimizu, T., Otsubo, M., Kato, Y., et al.: 2004, In: Mather, J.C. (ed.) *Optical, Infrared, and Millimeter Space Telescopes*, *Proc. SPIE* **5487**, 1142.

Ichimoto, K., the Solar-B Team: 2005, *J. Korean Astron. Soc.* **38**, 307.

Ichimoto, K., Shinoda, K., Yamamoto, T., Kiyohara, J.: 2006, *Publ. Natl. Astron. Obs. Japan* **8**, 11.

Kosugi, T., Matsuzaki, K., Sakao, T., Shimizu, T., Sone, Y., Tachikawa, S., *et al.*: 2007, *Solar Phys.* **243**, 3.

Shimizu, T.: 2004, In: Sakurai, T., Sekii, T. (eds.) *The Solar-B Mission and the Forefront of Solar Physics* **CS-325**, Astron. Soc. Pac., San Francisco, 3.

Shimizu, T., Nagata, S., Edwards, C., Tarbell, T., Kashiwagi, Y., Kodeki, K., et al.: 2004, In: Mather, J.C. (ed.) *Optical, Infrared, and Millimeter Space Telescopes*, *Proc. SPIE* **5487**, 1199.

Shimizu, T., Nagata, S., Tsuneta, S., Tarbell, T., Edwards, C., Shine, R., *et al.*: 2008, *Solar Phys*. in press.

Skumanich, A., Lites, B.W.: 1997, *Astrophys. J. Suppl.* **110**, 357.

Suematsu, Y., Tsuneta, S., Ichimoto, K., Shimizu, T., Otsubo, M., Katsukawa, Y., *et al.*: 2008, *Solar Phys.* in press.

Tarbell, T.D., *et al.*: 2008, *Solar Phys.* to be submitted.

Tsuneta, S., Ichimoto, K., Katsukawa, Y., Shimizu, T., Otsubo, M., Nagata, S., *et al.*: 2008, *Solar Phys.* in press.